Lab on a Chip

Devices and applications at the micro- and nanoscale

Accepted Manuscript

This article can be cited before page numbers have been issued, to do this please use: O. Walker, R. R. Benedix, J. Fischer, K. Hirzel, C. Stubenrauch and M. Heymann, *Lab Chip*, 2026, DOI: 10.1039/D6LC00261G.

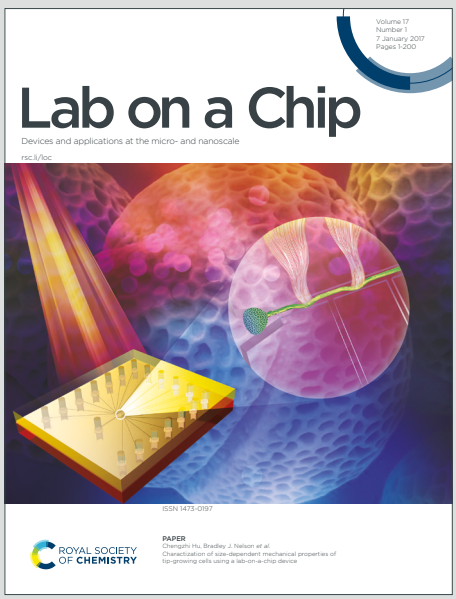




ROYAL SOCIETY OF CHEMISTRY

rsc.li/loc

Received 00th January 20xx,
Accepted 00th January 20xx
DOI: 10.1039/x0xx00000x



# Bridging dimensions: Combining one- and two-photon 3D printing for microfluidic device fabrication

Oliver Walker[a,b], Robin R. Benedix[b], Julian Fischer[b], Kai Hirzel[a], Cosima Stubenrauch[b], and Michael Heymann[a,*]

Additive manufacturing has been invaluable for 3D microfluidic integration. We combine high-resolution two-photon printed microfluidic features with fast one-photon printing to reduce overall fabrication time by about 20fold without compromising the accuracy of performance critical features. Alignment strategies and interface design tolerances ensure fluidic sealing and the reproducible assembly between both 3D printing techniques. The resulting devices produce highly monodisperse GelMA-based foams with a polydispersity index of below 5 % and tunable bubble radii between 235 to 400 µm. Combining multiple print modalities into a unified fabrication workflow will harness efficiency gains by utilizing high precision only where necessary.

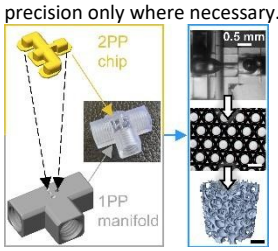


## 1. Introduction

Microfluidic miniaturization has inspired countless lab-on-a-chip technologies that manipulate and control small amounts of fluids ($10^{-9}$ - $10^{-18}$ L) in channels with dimensions from hundreds down to a few micrometers[1,2], or even nanometers[3]. As sample material has to be introduced into the microchannels at the correct place and time, a wide range of micro-macro interfaces have been developed, such as pumps to move fluids through connectors and tubing[4]. In 1992, this interfacing was realized by inlet and outlet holes drilled into a silicon chip into which pipette tips carrying the liquid samples for analytical chemistry were mounted.[5] Since then, microfluidics expanded to also include bioanalysis[6], to screen protein crystallization conditions[7-9], drug development[10], organ-on-a-chip systems[11,12], or monodisperse foam and emulsion formation[13-18], to name a few. These diverse applications, with different degrees of device complexity benefit from complementary engineering solutions that help bridge the dimensional gap between a macroscopic sample reservoir and a microchannel.

Common device manufacturing such as soft lithography, photolithography or injection molding interface the chip via punched or drilled holes[19,20]. Such ports are subsequently coupled to external tubing or fittings using adhesive bonding, mechanical clamping, or standardized connectors[19,21]. In soft lithography most of the fabricated microfluidic devices consist of Polydimethylsiloxane (PDMS), an elastic, fairly inexpensive, and optically transparent polymer[22]. Further, the elastic nature of PDMS has been exploited to directly integrate pumps and/or valves into the microfluidic chip[23,24]. Glass, silicon[25], or thermoplastics in turn have been preferred for their higher solvent resistance, rigidity or to reduce evaporative solvent loss from microchannels through their device walls. While initially realized as 2D devices through photolithography or micromachining[25], additive manufacturing has increasingly been able to process these different materials[26], affording new opportunities for microfluidic engineering.

Numerous photopolymerization based 3D printing techniques are available for microfluidic device fabrication, with a trend to decreasing costs, increasing precision, and material variety. In stereolithography (SLA), a focused light spot is guided through a photosensitive resin to locally polymerize the material. As a consequence, fabrication rates scale with focus spot size and scan speed. Digital light processing (DLP) in turn can cure one complete layer in a single exposure, to increase overall volume fabrication rates. For simplicity, we refer to both as one photon polymerization (1PP). Commercial SLA/DLP systems operate with lateral XY resolutions down to 25 - 50 µm and adjustable layer thicknesses [27], while custom high-resolution DLP-SLA systems with 7.6 µm lateral resolution and 6 - 10 µm layer thicknesses have been reported[28]. SLA and DLP hence reach fairly high precision, as required for droplet nozzles to formulate monodisperse emulsions[29-31]. A common limitation, however, pertains to surface roughness which adversely affects optical transparency of a device, but also fluid flow stability. Two-photon polymerization (2PP), also commonly referred to as two-photon stereolithography or direct laser writing, offers a few hundred nanometer lateral XY and about 1 µm longitudinal Z resolution[32]. These specifications result in very smooth surfaces and high-resolution free-form features, for example for nanoliter cell culture perfusion assays[33], or to form sub-micrometer liquid jets for free-electron femtosecond crystallography sample delivery[34]. While 1PP can achieve fabrication rates exceeding $cm^3$/hr, 2PP is predominantly limited to below a $mm^3$/hr. Choosing an optimal 3D printing technology for a specific microfluidic device thus amounts to finding the right trade-off between required resolution and overall fabrication rates.

Additive manufacturing of microfluidic devices ideally combines faster, low-resolution printing for uncritical features with slower, high-resolution printing for critical features in a simple process. This would achieve the highest design freedom and functionality while saving time, as the slower high-resolution process is limited to as few features as necessary.

[a] Institute of Biomaterials and Biomolecular Systems, University of Stuttgart, Stuttgart, Germany.
[b] Institute of Physical Chemistry, University of Stuttgart, Stuttgart, Germany.
Supplementary Information available: The data supporting this article have been included as part of the supplementary information (SI). See DOI: 10.1039/x0xx00000x

View Article Online
DOI: 10.1039/D6LC00261G

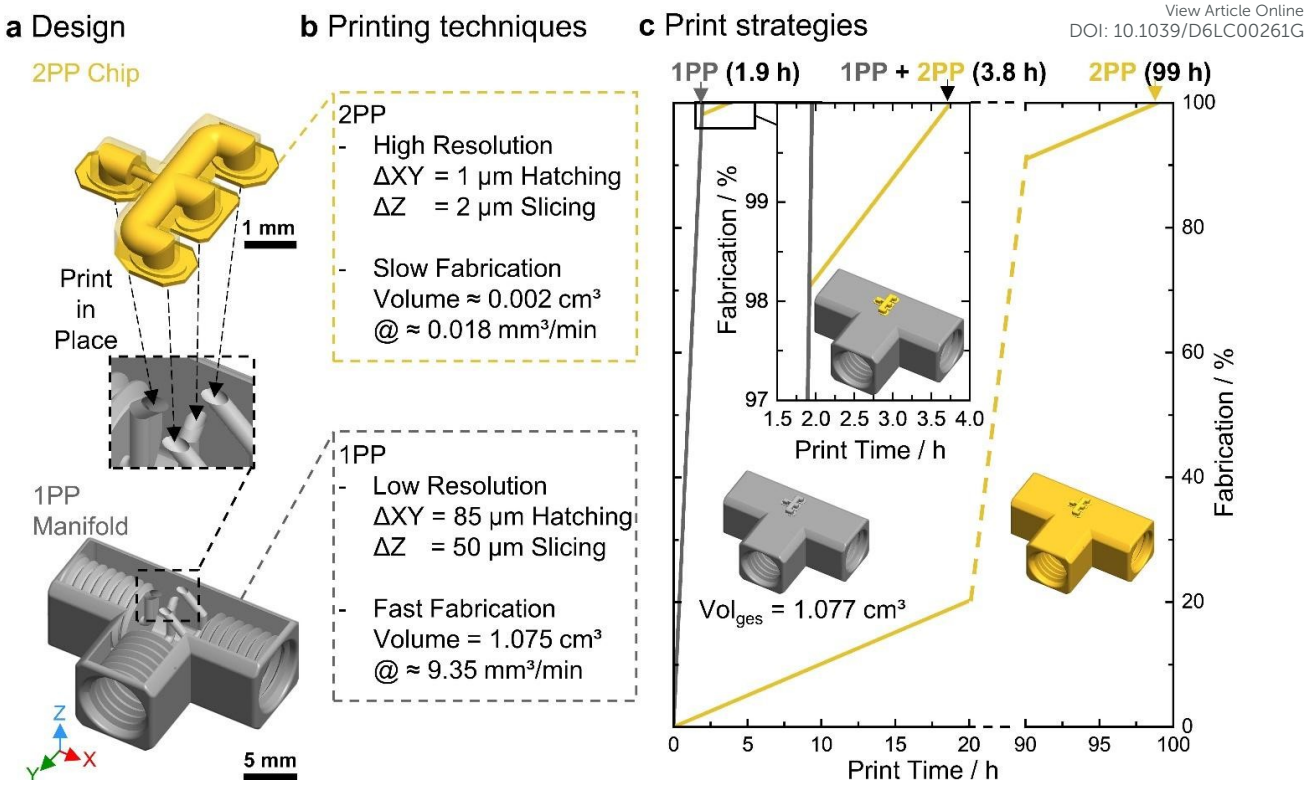


**Figure 1:** Design and *ex situ* 2PP microfluidic device manufacturing. (**a**) The device design comprises a 2PP chip that is printed onto a channel manifold realized via 1PP printing. (**b**) Slow, high resolution 2PP is restricted to the functional element, while fast, low resolution 1PP is used for the larger manifold. (**c**) This combined 1&2PP printing approach reduces overall fabrication time to 3.8 h, or about 26-fold, as the 2PP print would require 99 h.

Such hybrid approaches have been classified into four cases[4]: (1) The "master mold fabrication" approach fabricates high-resolution molds with 2PP for PDMS soft-lithography[35-38]. Molded replicas are then interfaced by punching or drilling inlet and outlet ports. (2) The "substrate integration" approach comprises 2PP microstructure manufacturing on planar surfaces, which are subsequently enclosed into PDMS or 1PP channels with fluidic interconnects[39-41], or sealed by mechanical clamping [42]. (3) "*In situ* 2PP" prints features directly into prefabricated microchannels[43,44] to realize for instances microvessel-like channels with inner diameters below 10 µm, microfluidic transistors with 500 nm walls, and soft microactuators in enclosed channels[45,46]. (4) "*Ex situ* 2PP" prints microstructures on existing fluidic components, such as glass capillaries or tubing connectors[34,47-49]. Here the 2PP printed part itself closes the fluidic circuit. While conceptually elegant, *ex situ* 2PP is less forgiving, as poor substrate alignment and fluidic sealing impede process reproducibility. Alternatively, fabrication time optimization explored one-photon pre-sensitization to lower the 2PP polymerization threshold and hence exposure times[50], or differential 2PP voxel placement for photonic[51] and ultracompact 3D microfluidics[34]. Also, hybrid instruments, that combine two optical engines with select low- and high-resolution have been reported[52,53]. Taken together, numerous approaches have sought to overcome the resolution fabrication rate trade-off, but have not yet matured into routine process nodes.

In this work, we manufacture a bubble-producing microfluidic device in an *ex situ* 2PP workflow that integrates a 1PP fluidic manifold to balance resolution requirements and fabrication rates (**Figure 1**). Furthermore, the manifold design and print process is optimized for alignment reproducibility and fluidic sealing. The 1PP manifold integrates threaded ports to connect to fluid delivery and provides a channel interface to receive high-resolution 2PP features. A customized and reusable 1PP adapter positions the manifold for accurate XY alignment and Z interface leveling. In a proof-of-principle example, gelatin methacryloyl (GelMA) foams with bubble radii ranging from around 225 - 400 µm are produced by this combined 1&2PP microfluidic device for future applications in controlled drug release. This strategy presents a time-saving, reproducible microfluidic device fabrication workflow with full 3D design space freedom while utilizing high precision only where necessary.

## 2 Results and discussion

### 2.1 1PP process and interfacing inform manifold design

We set out to engineer a nozzle for liquid foam templating that is about 1 $cm^3$ in size and that combines both 1 and 2PP microfabrication in an optimal way. The available volume fabrication rates of the 1PP machine were approximately 9.35 $mm^3$/min and 0.018 $mm^3$/min for 2PP microfabrication (**Figure 1b, c**). In a first step, the smallest reliably printable channel dimensions were determined for the 1PP printer (**Figure 2**). Available microchannel dimensions in the 1PP manifold define the connection interface to the 2PP chip. Nominally, our 1PP SLA printer specified 85 µm pixel sizes and 50 µm layer thickness. Following these parameters, we fabricated test-channels ranging from 0.1 – 0.9 mm with 0.1 mm increments and a length of 7.5 and 15 mm (**Figure 2, S1**). A sample tilt (x = 39° and y = 21°) was used to distribute print layer steps over a larger area, to in turn reduce staircase artefacts and to improve feature resolution. At this tilt, channels were manufactured either "downwards" (blue) or "upwards" (orange) (**Figure 2b**). Microscopic evaluation of the resulting channels implicated diameters below 0.6 mm as prone to clogging and diameters of 0.2 mm as unresolvable (**Figure 2c**). These cutoff values were similar for downward or upward print direction and agreed with previous reports working with the same hardware and resins[54,55]. Furthermore, channel conformity between design and printed channel diameters decreases strongly below 600 µm diameter. Fabricating the desired nozzle orifices of 200 µm with the 1PP machine alone was therefore not possible.

With the *ex situ* 2PP approach in mind, we intended to implement a 1PP manifold with 800 µm diameter channel sizes that can reliably be fabricated with the available 1PP process (**Figure 3a, S2**). To limit the required 2PP chip footprint, four of these 800 µm channels were routed into a connection zone of about 3.2 x 4.1 mm on one side of the manifold (**Figure 3, S2**). Here, the 1PP process limits the later 2PP chip miniaturization and in turn manufacturing time reduction, as both interface dimensions have to be reconciled. Three access ports for continuous liquid phase and disperse gas phase injection and an outlet were realized as standard right-handed threaded 1/4-28 UNF connectors to sample reservoirs (**Figure S2**). The 1/4-28 thread was chosen, as its 907 µm thread pitch matched well to the previously determined 1PP channel resolution target.

Second, to specify the correct flange design height (Z) for the 2PP chip, the surface roughness of the connection port interface was evaluated (**Figure 3b**). For this, the height profile of the 1PP manifold was recorded by multiphoton microscopy and analyzed with a custom Python script (**SI Section S2**). The maximum areal peak height on the connection port interface was $S_p$ = 55 µm, while the maximum profile peak height in the X cross section and the Y cross section were $R_p$ = 42 µm and $R_p$ = 32 µm, respectively. The arithmetical mean surface roughness of the port interface was $S_a$ = 13 µm (**Figure 3b, Table S1**). Given these roughness values, we chose a 100 µm thick flange to ensure gap free interlocking between the rougher 1PP manifold and the finer 2PP chip (**Figure S2, S3**). Furthermore, this flange height elevates all microchannels inside the 2PP chip safely above possible 1PP surface obstructions.

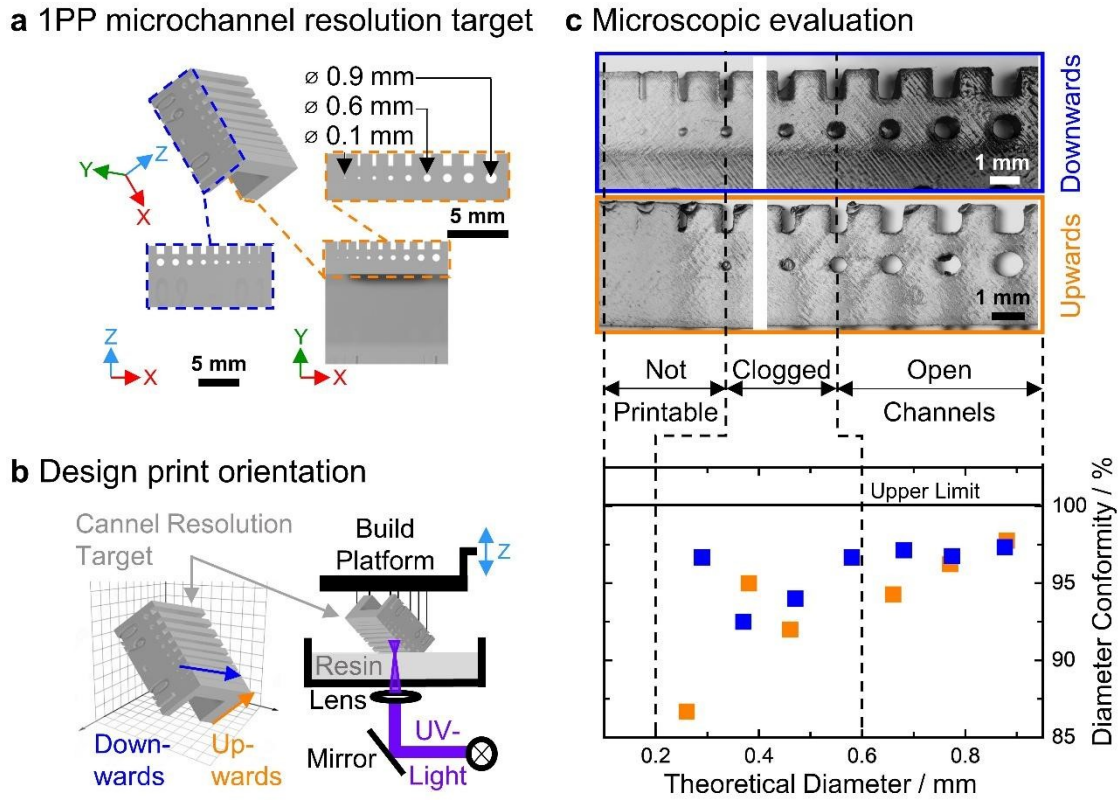


**Figure 2**: 1PP channel resolution target revealing the channel diameter print limit. (a) 1PP channel resolution target covers channel diameters ranging in 0.1 mm steps from 0.1 to 0.9 mm. (b) 3D print space alignment with a rotation of 39° in X and 21° in Y yields general higher precision and results in a downwards (blue) and upwards (orange) channel orientation. (c) Microscopic diameter conformity between the as designed channel diameters and actual printed diameters. Below a designed diameter of around 600 µm the channels tend to clog and are not printable at all below ⌀ = 200 µm.

View Article Online
DOI: 10.1039/D6LC00261G

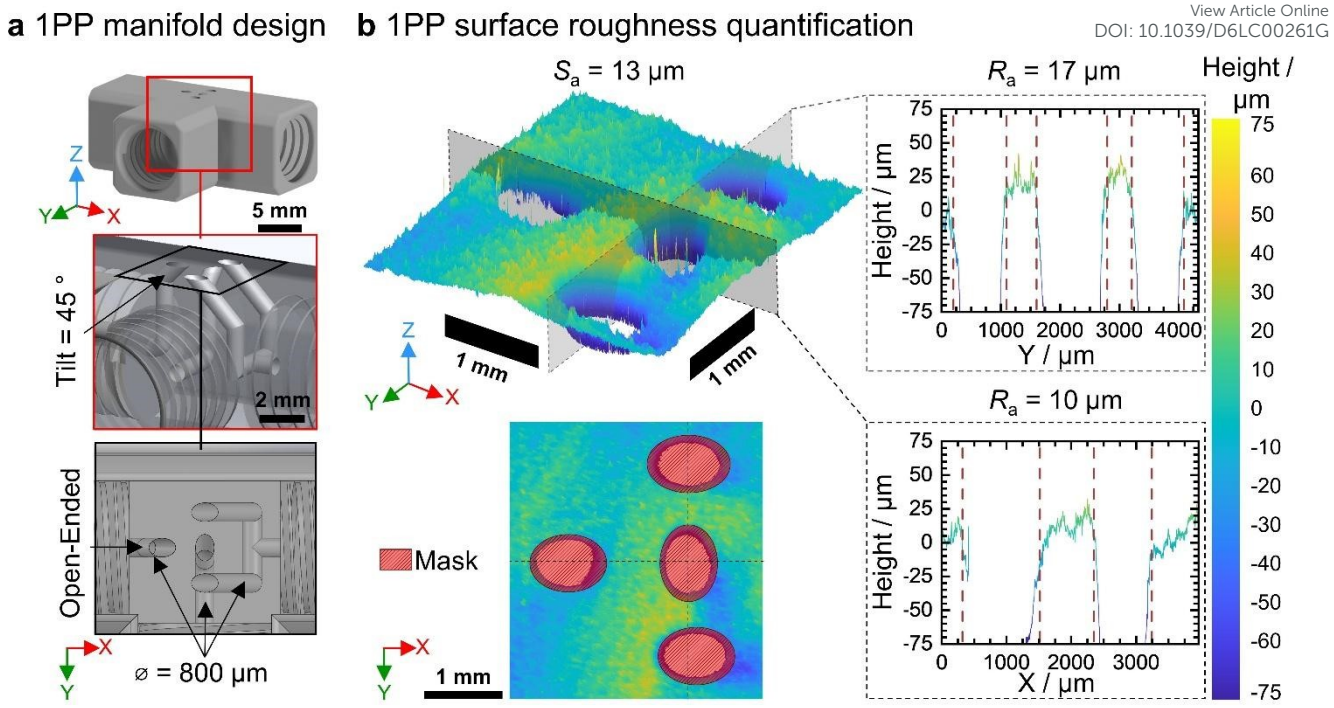


**Figure 3:** 1PP manifold design and surface roughness analysis of the microchannel interface. (**a**) The 1PP manifold routes 800 µm channels at a 45° angle relative to the surface to interface with the precise 2PP chip. Manifold inlets were realized as 1/4-28 UNF threaded connectors to mount liquid and gas supply lines. (**b**) Surface roughness analysis revealed highs and lows of order 50 µm above and below the mean surface. Areal and profile plots show the unmasked data while it is considered in the given values. Note, the ellipsoidal shape is a consequence of the 45° angle of the channels.

### 2.2 2PP chip design and integration with 1PP manifold

The 2PP chip connects to the four access channels in the 1PP manifold with an adapter flange with sufficient alignment tolerances of 300 µm ΔX, 170 µm ΔY and 100 µm ΔZ to facilitate a good seal (**Figure 4b**, **S3**). For this, a 1PP adapter was tailored to help place the 1PP manifold in the sample holder of the 2PP printer (**Figure 4, S2, S4**). To firmly mount the 1PP manifold, the cavity in the adapter design was pre-compensated to 8.15; 21.55 mm in X and 8.7; 15.8 mm in Y direction. A pre-compensation of 25.4 and 25.25 mm afforded a tight fit of the adapter in the 2PP sample holder (**Figure 4a, S2, S4).** This anisotropic rescaling was required because of the tilted print direction of the respective parts. Clips were included with the adapter so that it could hang securely in the inverted sample position in the 2PP printer. Note, the permissible overall height of the combined adapter and manifold is limited to below the effective Z-stage travel range of about 10 mm of the 2photon lithography machine.

The main channels in the 2PP chip had diameters of 600 µm and were enclosed in a 100 µm thick wall, resulting in a total nozzle device volume of 0.002 $cm^3$ (**Figure 1**). Such stringent reduction of unnecessary bulk device volume minimizes the slower, high precision 2PP print time. The flow-focusing X-junction was realized with nominal constriction diameters of 250, 350, and 500 µm and a length of 500 µm (**Figure S3**). Isotropic shrinkage during development resulted in constriction diameters of about 240, 340 and 480 µm in the final part. For fabrication, the 2PP chip was split into multiple blocks to accommodate the 800 x 800 µm field of view of the used 10x writing objective. Blocks were distributed such that the constriction remained clear of block edges and hence possible block stitching artifacts (**Figure 4b**). 2PP chip fabrication consisted of four steps (**Figure 4a**, **S7a-d**): (1) all manifold inlets are sealed with polyimide adhesive tape, (2) the manifold is then placed in the adapter, (3) which is then placed into the 2PP sample holder, before (4) three drops of IP-S resin with a total volume of about 150 µL were added. The first two drops were needed to prefill the microchannels at the 1&2PP interface. With the third drop enough resin was deposited to complete the full print in dip-in immersion mode.

The initial print start position was confirmed manually. No rotational compensation was required and XY coordinates rarely required adjustments, confirming the chosen tolerances and the reliable manifold positioning of the adapter. In contrast, initial Z-placement of the first block was observed to be a critical parameter. Z-positioning was adjusted manually in two steps. First, the channel edge surface was moved into focus, and second, the focus was shifted 40 µm deeper in the 1PP manifold. This achieved a stable fluidic seal between both parts. We hence chose the central block as the first print block.

After developing (**Section S3**, **Figure S7**) the chip could be used as intended, but the substantial surface roughness of the 1PP manifold together with the curved channel geometry in the 2PP chip compromised visibility of the inner nozzle. To provide a clean interface for microscopy, a glass coverslip was glued over the 2PP chip with a drop of 1PP resin (**Figure 5**). Apart from enhancing optical transparency, this also improved mechanical stability of the resulting device.

View Article Online
DOI: 10.1039/D6LC00261G



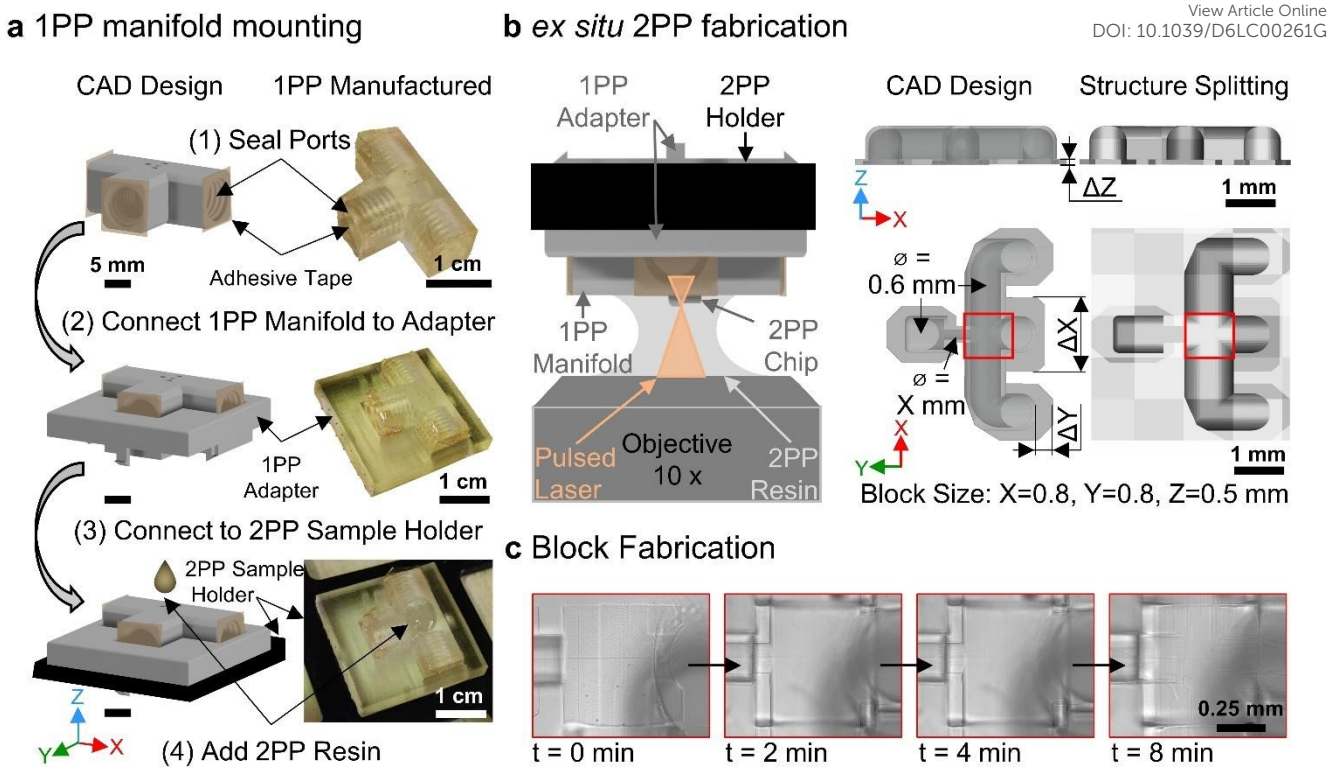


**Figure 4**: 1PP Manifold preparation for aligned 2PP chip fabrication. (**a**) The 1PP manifold inlet ports were (1) sealed with adhesive tape prevent 2PP resin flow into the channels during printing. The manifold was then (2) mounted with a custom adapter into (3) the 2PP sample holder, before (4) 2PP resin is added onto the interface zone. (**b**) Schematic of *ex situ* 2PP chip fabrication in dip-in mode. The 2PP chip was design for alignment tolerances of ΔX = 300, ΔY = 170 and ΔZ = 100 µm to yield a strong leak free connection to the 1PP manifold without dedicated manual alignment. The orifice for bubble formation in a X-junction configuration had a as designed diameter of X = 250, 350, 500 µm. As the 2PP chip exceeded a field of view of the 10x writing objective, the chip was split into blocks of 800 µm², which each required approximately 8 minutes print. All important features were placed into a single block to avoid stitching artefacts to degrade bubble formation. (**c**) Brightfield microscopy shows the 2PP progress of the central hatching block with the nozzle orifice.

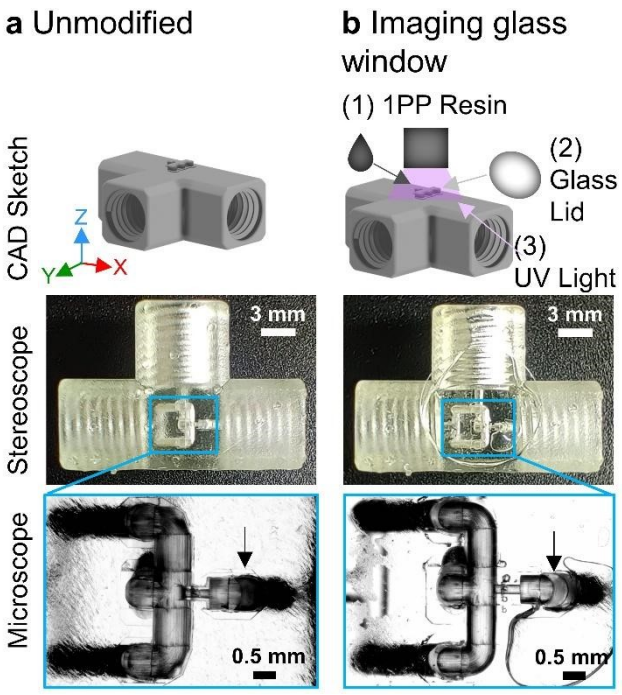


**Figure 5**: Improved optical transparency via glass coverslip lidding. (**a**) While the 2PP chip was operational as printed, curved microchannels and manifold surface roughness impede visibility of bubble formation (black arrow). (**b**) Adding a glass window help resolve bubble break-up dynamics.

### 2.3 Microfluidic bubble generation setup

For functional characterization of the 2PP chip, monodisperse liquid foams were generated from a continuous phase of an aqueous GelMA/photoinitiator/surfactant solution (**Figure 6, S8, Video S1**). Injected gas is squeezed through the nozzle constriction leading to bubble formation when conditions for the squeezing regime are met[56]. The smooth surface and dimensional accuracy of the high resolution 2PP manufacturing prevent undesired turbulences and facilitates reproducible bubble production. For instance, the 240 µm diameter orifice produced a 260 µm diameter bubble every ~ 28 ms, for a liquid flow rate of 100 µL $min^{-1}$ and a gas pressure of 60 mbar (**Figure 6b, Video S1**). Together with two larger nozzle orifice sizes, bubbles of up to 400 µm diameter could be produced by adjusting the gas pressure. The observed monodispersity for each tested condition was high, with all PDI values < 5%. In a final step, highly ordered liquid foam templates were UV-crosslinked into micro-structured gelatin-based hydrogels, resulting in pore radii of ~200 - 450 µm (**Figure 6b,** bottom right). These porous gelatin-based hydrogels are part of an ongoing project in which they are compared to gelatin-based hydrogel particles with radii between 50 and 100 µm in terms of their drug sorption and release behavior[57]. For this comparison, the bubble templates used here are intended to yield porous hydrogels in which the node dimensions, i.e. the regions where several pores meet, are comparable to the hydrogel particle diameter, such that characteristic diffusion lengths remain in a similar range.

View Article Online
DOI: 10.1039/D6LC00261G

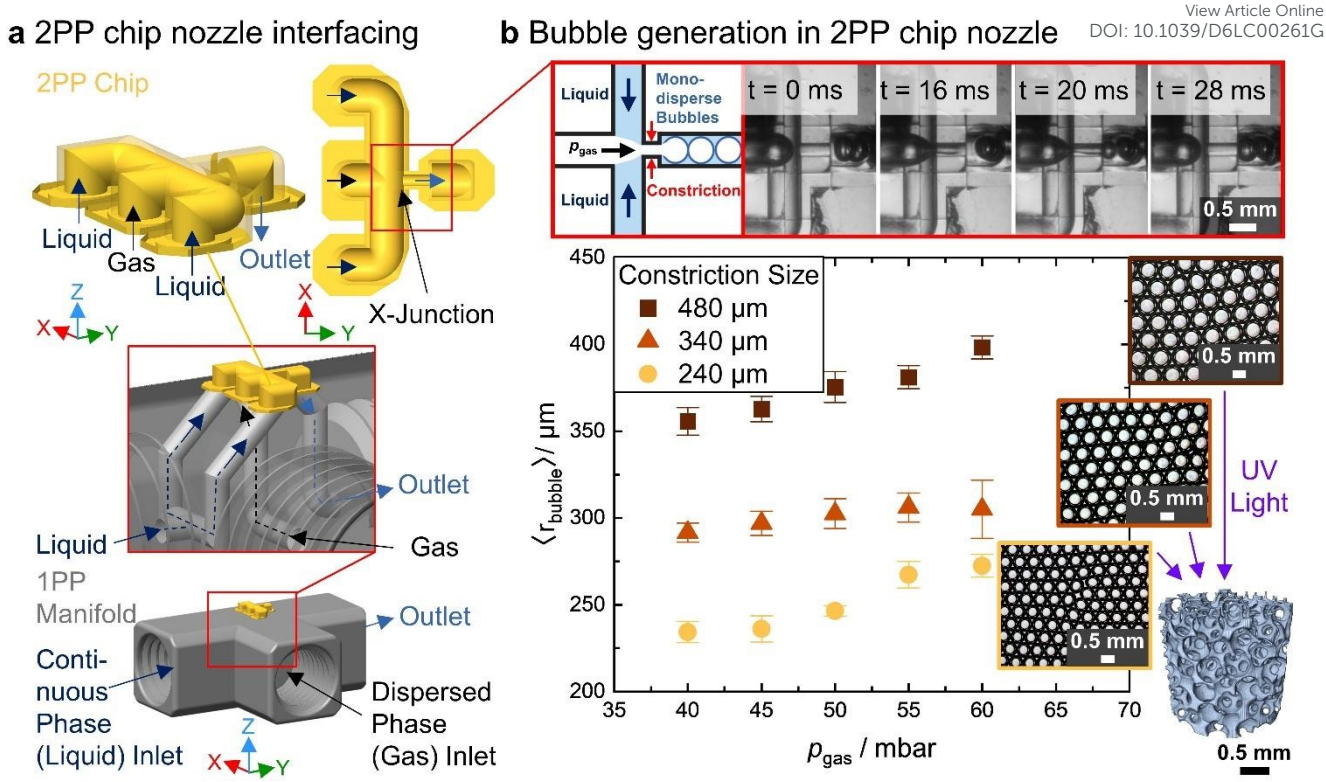


**Figure 6:** Connection and quantification of the microfluidic device for bubble production. (**a**) The 1PP manifold supplies continuous and dispersed phase reservoirs into the 2PP chip. (**b**) $N_2$/perfluorohexane bubbles in a continuous aqeous GelMA/photoinitiator/surfactant phase form at nozzle constriction within the 2PP chip at a rate of approximately ~35 Hz. The mean bubble radius, $\langle r_{bubble} \rangle$, increases with gas pressure, $p_{gas}$, and for larger constriction size. Photochemical crosslinking yields highly monodisperse liquid foams of porous gelatin-hydrogels.

### 2.4 Harnessing high-resolution 2PP features

While the targeted gelatin hydrogel application[57] operated comparably large 2PP features, we evaluated whether the process could also achieve smaller internal features as previously demonstrated with *in situ* 2PP[45,46]. As an example, we included microfilter meshes in the inlet ports (**Figure 7a**). The mesh was rescaled from the published design jkmh #7[34] to a mesh width of 90 µm with strut dimensions of 9 × 13 µm. Operating with the previously established 2PP settings resulted in intact filter meshes after development. Similar micromeshes, but also finer grids, could support flow conditioning or prevent aggregates from reaching and clogging the nozzle. Next, we reduced the nozzle constriction to 50 µm diameter to yield smaller microbubbles (**Figure 7b**). At a liquid flow rate of 10 µL $min^{-1}$ and a gas pressure of 40 mbar, approximately 30 µm diameter gas bubbles were produced (**Video S2**). Both examples confirm that the workflow can be readily extended down to higher resolution features unique to 2PP.

## 3 Conclusion

Bridging the dimensional gap between functional microchannel features and macroscopic fluidic interfaces is a classic challenge in microfluidic engineering. We present an *ex situ* 2PP workflow to realize microfluidic devices that combine faster, but low resolution 1PP SLA and slower, high resolution 2PP direct laser writing. While ultracompact 2PP microfluidic nozzles have been shown before, including modular assembly strategies [33,58], they still required extensive manual assembly work. The 1PP manifold provides a convenient fluidic interface to syringe pumps and pressure controllers without compromising resolution of the 2PP chip or bloating fabrication time.

Reproducible alignment between 1PP manifold and 2PP chip is facilitated by an adapter configured for suitable fabrication tolerances. This adapter strategy could support batch processing in the future. Up to 9 adapters could be placed on the current 2PP sample holder to fabricate as many chips in a single overnight production run (9*1.9 h = 17.1 h). Alternative holders in combination with high resolution 1PP manifold prefabrication could further increase throughput by further miniaturizing the 1&2PP interface and in extension also the 2PP chip. Moreover, an alignment based on automated image recognition could reduce design tolerances, further decreasing 2PP fabrication volume and thus time and cost.

As an application for the 2PP chip, we demonstrate a flow focusing bubble nozzle to formulate GelMA-foams[18]. Self-assembled foam templates yield highly structured porous gelatin hydrogels upon polymerization. Compared to bulk hydrogels, such macroporous architectures provide enhanced surface area and defined diffusion pathways that are crucial for drug release applications [18,59]. The precise control over bubble formation within the microfluidic device directly translates into tuneable hydrogel pore size and network connectivity, enabling tailored mass transport. Thus, this level of structural control relies on reproducible bubble generation, which in turn depends on nozzle precision, surface quality, and stable flow conditions, all of which we addressed in the presented fabrication strategy.

Numerous other microfluidic nozzle configurations have successfully been implemented as 1PP or 2PP printed monoliths[60,61]. As technical improvements will increase 1PP

View Article Online
DOI: 10.1039/D6LC00261G

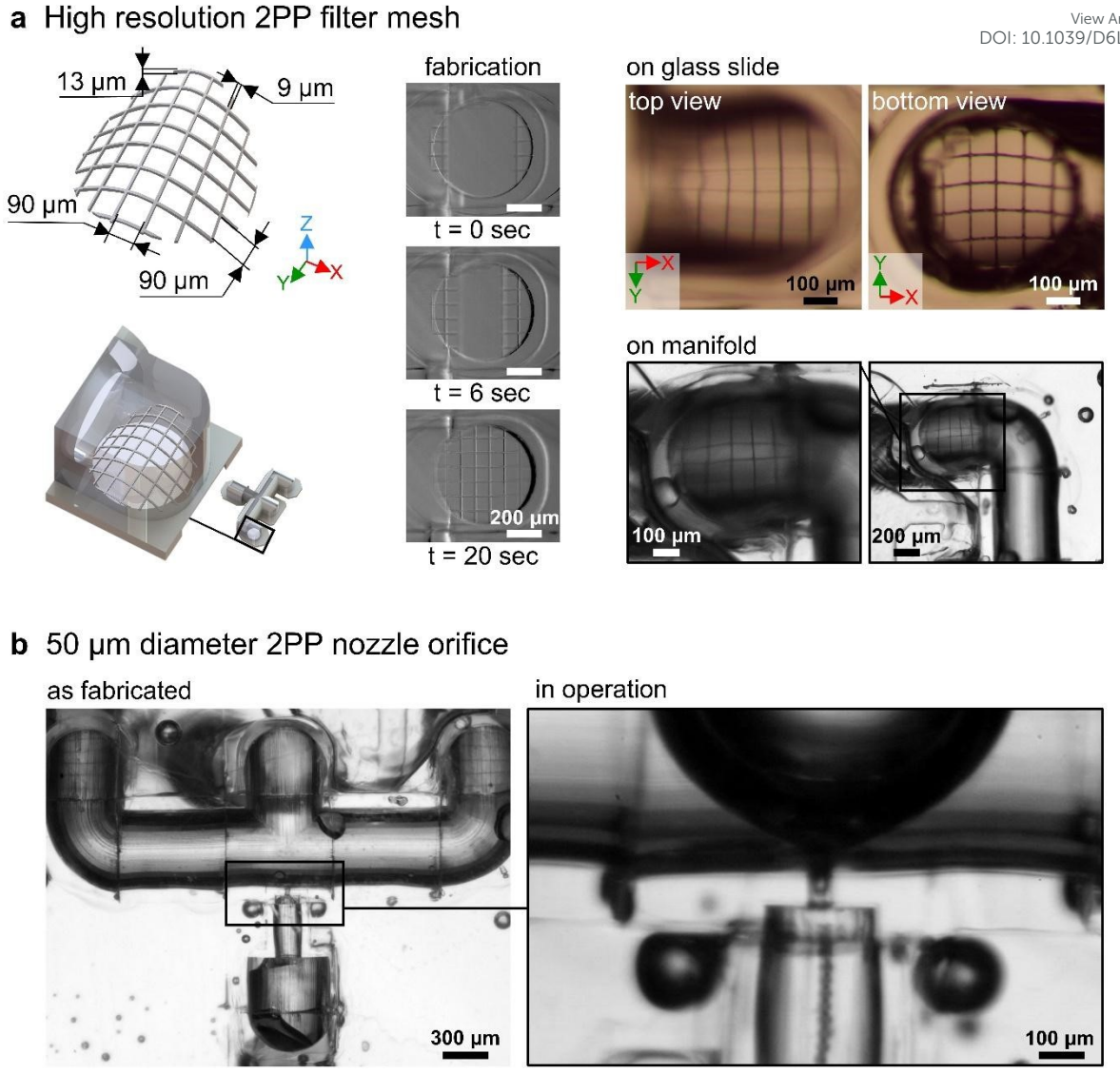


**Figure 7**: Fine feature demonstration. **(a)** Filter mesh with 9 × 13 µm strut segments of 90 µm mesh width printed in about 20 seconds. Filter meshes were stable during fabrication and after development. For quality control, a filter segment was directly printed onto a glass slide to microscopically evaluate it from both sides. **(b)** Meshed 2PP chip design with a 50 µm diameter constriction readily developed with the default process and reliably produced bubbles with a liquid flow rate of 10 µL $min^{-1}$ and 40 mbar gas ($N_2$) pressure.

resolution[62,63] or 2PP volume print rates[64], the optimal cross-over point between both techniques will drift in favour of the former or the latter. Notwithstanding, combining different additive manufacturing techniques via a unified sample holder into a unified process affords interesting opportunities for microfluidic engineering, as mutual strengths can be reinforced and each other's weaknesses complemented. We expect the 1&2PP process integration shown here to be especially advantageous for optofluidic integration. 2PP has achieved remarkable success in realizing microoptical systems[65], which will help with large scale integration and real-time sample process monitoring, such as fluorescence activated cell and droplet sorting[66]. Different process windows and resolution targets could equally benefit from the specific *ex situ* 3D printing integration as presented here, especially for integrating multiple materials, such as organ-on-chip systems where 3D hydrogel cell-culture scaffolds are cultivated under perfusion[67]. The versatile platform developed here represents a generalizable methodology to seamlessly bridge dimensions to achieve custom devices and architectures.

## 4 Material and Methods

### 4.1 Computer aided design

CAD files were designed in SolidWorks 2022 (Dassault Systèmes) and exported in surface tessellation language (STL) file format. The 1PP channel resolution target contained channels from 0.1 to 0.9 mm diameter in 0.1 mm increments (**Figure 2a**, **S1**). The 1PP manifold is 21 mm long, 14.5 mm wide, and 8 mm high (**Figure 3**, **S2**). Three threaded holes (1/4-28 UNF, right-handed thread with a depth of 9.25 mm) provide a mechanical interface to a fluid pump supplying liquid. The microchannels to interface with the 2PP chip have diameters of 800 µm and are oriented at 45° relative to the interface between 1 and 2PP. Further, the microchannel for liquid transport is divided within the 1PP manifold into two channels, reducing the necessary interfacing ports. Narrow open-ended channels for X-junction channel geometry are realized by placing the microchannel for gas transport below the liquid

microchannel so that it ends between the two ends of the liquid channel (**Figure S2**).

The 2PP chip is designed to cover the 1PP manifold and is 4.1 mm long, 3.23 mm wide, and 0.75 mm high (**Figure 4**, **S3**). Fluidic X-junction geometry channels for bubble production have a diameter of 600 µm, with as-designed nozzle diameters of 500 µm, 350 µm, or 250 µm. The total fabrication time of the 2PP chip is minimized by encasing all microchannels with a 50-100 µm thin wall.

The 1PP adapter (**Figure 4a**, **S4**) is 25.4 mm long, 25.25 mm wide and 6.5 mm high, with cavity design tolerances against the 1PP manifold of ~0.7; 1.3 mm ΔY and ~0.15; 0.55 mm ΔX to provide a snug fit while permitting removal of the manifold without excessive force. Visibility of the 1PP manifold surface is enhanced by an 11 mm long and 8.7 mm wide window in the cavity. Clips at the adapter bottom allow the adapter to connect to the 2PP sample holder (Nanoscribe), enabling easy removal and subsequent reuse (**Figure S7**).

### 4.2 1PP SLA fabrication

All 1PP was performed on a Form 3L equipped with two 405 nm, 250 mW lasers with a laser spot size of 85 µm in clear V4 resin (both Formlabs). Layer thickness (slicing) was set to 50 µm in PreForm software version 3.331 (Formlabs), using default settings of 35 °C resin temperature, 31 mJ $cm^{-2}$ exposure for perimeter, surface, and model filling and a 1s layer curing time after laser processing. An average print speed of 9.35 $mm^3$ $min^{-1}$ was inferred assuming a linear fabrication rate. The 1PP channel resolution target and the 1PP manifold were fabricated with 39° X and 21° Y tilt, while the 1PP adapter was oriented at 90° X direction relative to the build platform (**Figure S6**). Necessary support structures were added as shown in **Figure S6**, while omitting all critical fitting surfaces. Printed samples were gently lifted off the build platform using a spatula and removed from the supports. During post-processing, samples were (i) washed for 15 minutes in isopropanol in a stirred FormWash tank at 20 °C, (ii) dried under a stream of $N_2$ with a focus on blowing uncured resin out of the microchannels, and (iii) UV-cured for 10 minutes in a FormCure (UV light at 405 nm) preheated to 60 °C. Finally, fabricated 1PP manifold dimensions were measured using a caliper (accuracy ± 0.01 mm) to inform 1PP adapter cavity dimensions.

### 4.3 Multiphoton microscopy for 1PP manifold surface roughness evaluation

The manifold was stained for 5 h in 40 mL of 50 vol% (v/v) aqueous ethanol containing 1.6 mM rhodamine B (all Sigma Aldrich). Stained 1PP manifolds were imaged on a Stellaris8-DIVE multiphoton microscope equipped with a HCPL Fluotar 10× 0.4 NA objective (LEICA) and an InSightX3 (Spectra Physics). Rhodamine B was excited at 1200 nm. The surface of the manifold was rasterized over a 6 × 5 × 190 µm grid (X,Y,Z) using 1024 × 1024 pixel images with an effective pixel size of 1.14 × 1.14 µm and a step size of 1 µm in Z-direction, a 600 ns pixel dwell time and a 1.05/s frame rate. Images were stitched along the X- and Y-direction and cropped to the region of interest around the channel openings, resulting in a final image size of 4 x 4.3 mm.

The obtained images were converted into an 8-bit greyscale by a custom FIJI[68] macro and further processed using a custom MATLAB script. Greyscale value profiles of XY pixel combinations were then analyzed as a function of height (Z). The surface height was calculated relative to the center of mass of the height distribution, $z_{com}(x,y)$ (**Figure S5**). A lower cutoff value of 4% of the maximum greyscale value at $z_{com}(x,y)$ was chosen to suppress background and out-of-focus contributions. The cutoff as 4% was selected, as it represents the lowest threshold at which a plateau of $S_a \approx 13$ µm (arithmetical surface mean height) is reached (**Figure S5b**). The plateau indicates convergence of the reconstructed surface height. Using this cutoff, $z_{com}(x,y)$ was determined for all pixels and used to compute the surface parameters (**Section S2**). The center of mass of the greyscale value profile $z_{com}(x,y)$ was plotted against X and Y, resulting in a 3D representation of the manifold surface. Subsequently, the areas around the channel openings were masked to determine the midplane $z_{mean}(x,y)$ of the surface. Surface roughness was quantified in terms of the two-dimensional arithmetical surface mean height $S_a$ by integrating the absolute height difference $|z_{com}(x,y) - z_{mean}(x,y)|$ over the whole unmasked surface, according to

$$S_a = \frac{1}{A} \iint |z_{com}(x,y) - z_{mean}(x,y)| \, dxdy,$$

with the area of the unmasked surface $A$, the maximum surface height $S_z$, the maximum surface peak height $S_p$, and the maximum surface valley height $S_v$ (**Section S2**).

The surface was also analyzed by cuts through the channel openings and along the X- and Y-direction. The one-dimensional arithmetical profile mean height $R_{a,x}$ or $R_{a,y}$ along these cuts was calculated by

$$R_{a,x} = \frac{1}{l} \int |z_{com}(x,y) - z_{mean}(x,y)| \, dy, \text{ and}$$

$$R_{a,y} = \frac{1}{l} \int |z_{com}(x,y) - z_{mean}(x,y)| \, dx,$$

where $l$ is the length of the cut along the masked surface. Analogous to the two-dimensional case, the one-dimensional surface parameters, maximum profile height $R_{z,x}$ or $R_{z,y}$, maximum profile peak height $R_{p,x}$ or $R_{p,y}$ and maximum profile valley height $R_{v,x}$ or $R_{v,y}$, were calculated (**Section S2**).

### 4.4 2PP fabrication

The 2PP chip was fabricated in IP-S resin atop the 1PP manifold using a Photonic Professional GT2 equipped with a 10x 0.3 NA objective in dip-in mode (both Nanoscribe). A center wavelength around 780 nm with an output power < 180 mW and a 100 fs pulse duration and a repetition rate of 80 mHz were applied. STL design files were processed in Describe (Nanoscribe) using shell and scaffold mode, with the laser power set to 120 %, a 100 mm $s^{-1}$ scan speed, and 2 µm slicing and 1 µm hatching distances. The structure was split into rectangular blocks of 800 x 800 x 500 µm (X, Y, and Z) with a 10 µm XY and Z block overlap, respectively. After fabrication, the 2PP chip on the manifold was developed internally by connecting a 2 mL Luer-Lock tip glass syringe (Poulten & Graf GmbH) to the microfluidic 1PP manifold and flushing it using isopropanol to remove all uncured resin from the channels. In a second step, the microchannels were filled 3 times for 3 min each iterating between propylene glycol methyl ether acetate (PGMEA) (MicroChemicals GmbH) and isopropanol. In a final step, the channels were dried using pressurized air. All fabrication and post-treatment steps were performed in a cleanroom in the absence of UV light to prevent unintended resin curing and subsequent channel clogging (**Figure S7**). For printing time calculation, a linear fabrication rate was assumed.

Optical transparency was realized by placing a drop of clear V4 resin on top of the 2PP chip and gently pushing a glass coverslip (⌀ = 10 mm; thickness of 1 mm, Carl Roth GmbH + Co. KG) on the resin

View Article Online
DOI: 10.1039/D6LC00261G

drop. The complete assembly was then UV-cured for 10 min in a FormCure machine at room temperature.

#### 4.5 Microscopic evaluation of 1PP channel resolution target and 2PP constriction diameter

Parts were imaged with a SMZ 800 N bright-field microscope (Nikon) equipped with a MikroCam II camera (Bresser). Channel diameters were quantified in FIJI[68] and compared to design specifications as percentage diameter conformity.

#### 4.6 Microfluidic bubble generation

2PP chips with as-produced 240, 340, or 480 µm diameter nozzle orifices were used to generate liquid foams consisting of 20 wt% gelatin methacryloyl (GelMA), 0.14 wt% photoinitiator lithium phenyl-2,4,6-trimethylbenzoylphosphinate (LAP) (Merck KGaA), and 0.1 wt% surfactant Plantacare 2000 UP (BASF SE) in double-distilled water. GelMA was synthesized as previously reported[69]. An 11 elite syringe pump (Harvard Apparatus) controlled liquid flow, which was set to 100 µL $min^{-1}$. The gas phase consisted of $N_2$ with traces of perfluorohexane. The latter was added to the gas phase to stabilize the liquid foams against Ostwald ripening. Gas pressure was set by an OB1 MK1 pressure controller (Elveflow). A detailed schematic of the bubble generation setup is shown in **Figure S8**. Bubble formation inside the 2PP chip was imaged with a SMZ 745 T bright-field microscope (Nikon) and an EoSensCL high-speed camera (Microtron). Foam bubble monolayers were collected and imaged with a SMZ 800 N bright-field microscope (Nikon) and a MikroCam II (Bresser). A custom bubble detection Python script quantified bubble radii ($r_{\mathrm{bubble}}$), the mean bubble radius ($\langle r_{bubble} \rangle$) and the bubble radius distribution given by the polydispersity index as

$$PDI = \frac{\sqrt{\langle r_{bubble}^2 \rangle - \langle r_{bubble} \rangle^2}}{\langle r_{bubble} \rangle}.$$

## Author contributions

Oliver Walker: Conceptualization, Data curation, Formal analysis, Funding acquisition, Investigation, Methodology, Project administration, Software, Validation, Visualization, Writing – original draft, review & editing.
Robin Benedix: Data curation, Formal analysis, Investigation, Methodology, Visualization, Writing – review & editing.
Julian Fischer: Data curation, Formal analysis, Methodology, Software, Visualization Writing – review & editing.
Kai Hirzel: Data curation, Formal analysis, Writing – review & editing.
Cosima Stubenrauch: Resources, Supervision, Writing – review & editing.
Michael Heymann: Conceptualization, Resources, Project administration, Supervision, Visualization, Writing – original draft, review & editing.

## Conflicts of interest

There are no conflicts to declare.

## Data availability

The data supporting this article have been included as part of the supplementary information (SI). Supplementary information is available. See DOI:

## Acknowledgements

OW acknowledges funding from the University of Stuttgart via the Terra Incognita program. We thank Jakob Hoffmann for help and discussions about the 1PP channel resolution target, and Edgar Wolfert for providing the bubble detection Python script.

## References

1 G. M. Whitesides, *Nature*, 2006, **442**, 368–373;
2 S. Y. Teh et al., *Lab on a Chip*, 2008, **8**, 198–220;
3 Xu, Yan. *Advanced Materials*, 2018, **30**, 1702419;
4 O. M. Young et al., *Lab on a Chip*, 2024, **24**, 2371–2396;
5 A. Manz et al., *Journal of Chromatography A*, 1992, **593**, 253–258;
6 A. R. Wheeler et al., *Analytical Chemistry*, 2003, **75**, 3581–3586;
7 J. U. Shim et al., *Crystal Growth & Design*, 2007, **7**, 2192–2194;
8 B. Zheng et al., *Angewandte Chemie Int. Ed.*, 2004, **43**, 2508–2511;
9 M. Heymann et al., *IUCrJ*, 2014, **1**, 349–360;
10 P. S. Dittrich and A. Manz, *Nat. Rev. Drug Discov.*, 2006, **5**, 210–218;
11 S. R. Dabbagh et al., *Aggregate*, 2023, **4(1)**, e197;
12 H. Tolabi, et al., *Advanced Materials*, 2023, **35(26)**, 2208852;
13 C. Stubenrauch et al., *Angew. Chem. Int. Ed.*, 2018, **57**, 10024–10032;
14 J. Elsing et al., *Adv. Eng. Mater.*, 2017, **19**, 1700195;
15 M. L. Dabrowski et al., *RSC Adv.*, 2020, **10**, 8917–8926;
16 S. Andrieux et al., *Adv. Colloid Interface Sci.*, 2018, **256**, 276–290;
17 A. Quell et al., *Adv. Eng. Mater.*, 2015, **17**, 604–609;
18 F. Dehli et al., *Biomacromolecules*, 2019, **20**, 2666–2674;
19 Fredrickson & Fan, *Lab Chip*, 2004, **4**, 526–533;
20 N.Bings et al., *Analytical Chemistry*, 1999, **71(15)**, 3292–3296;
21 J. Wang, et al., *Lab on a Chip*, 2014, **14(10)**, 1673–1677;
22 J. C. McDonald et al., *Electrophoresis*, 2000, **21**, 27–40;
23 Y.-H. Lin et al., *JMEMS*, 2008, **17**, 573–581;
24 T. Thorsen et al., *Science*, 2002, **298**, 580–584;
25 D. J. Beebe et al., *Annu. Rev. Biomed. Eng.*, 2002, **4**, 261–286;
26 F. Kotz, et al., *Nature*, **2017**, 544(7650), 337–339;
27 H. Gong et al., *RSC Adv.*, 2015, **5**, 106621–106632;
28 H. Gong et al., *Lab Chip*, 2017, **17**, 2899–2909;
29 K. Ohtani et al., *J. Oleo Sci.*, 2014, **63**, 93–96;
30 J. M. Zhang et al., *RSC Adv.*, 2016, **6**, 81120–81129;
31 J. Zhang et al., *J. Food Eng.*, 2021, **290**, 110212;
32 C. M. Portela, C. M., *Nature Materials*, 2021, **20(11)**, 1491–1497;
33 H. J. McLennan et al., *Sci. Rep.*, 2023, **13**, 562;
34 J. Knoška et al., *Nat. Commun.*, 2020, **11**, 657;
35 A. C. Lamont et al., *Sci. Rep.*, 2019, **9**, 394;
36 C. Hu et al., *Lab Chip*, 2014, **14**, 2447–2455;
37 D. Barata et al., *Lab Chip*, 2017, **17**, 4134–4147;
38 R. Soffe et al., *Sens. Actuators B*, 2017, **251**, 963–975;
39 Y. Zhou et al., *Adv. Mater. Technol.*, 2020, **5**, 2000323;
40 M. Nouri-Goushki et al., *ACS Biomater. Sci. Eng.*, 2019, **5**, 6127–6136;
41 S. Grebenyuk et al., *Nat. Commun.*, 2023, **14**, 193;
42 M. Luitz et al., *Adv. Mater. Technol.*, 2023, **8**, 2300667;
43 L. Amato et al., *Lab Chip*, 2012, **12**, 1135–1142;
44 D. Wu et al., *Laser Photonics Rev.*, 2014, **8**, 458–467;
45 A. T. Alsharhan et al., *Lab Chip*, 2019, **19**, 2799–2810;
46 A. T. Alsharhan et al., *J. Micromech. Microeng.*, 2021, **31**, 044001;
47 E. Montinaro et al., *PLoS One*, 2018, **13**, e0192780;
48 A. Dewandre et al., *Sci. Rep.*, 2020, **10**, 21616;

View Article Online
DOI: 10.1039/D6LC00261G


**49** A. Barbot et al., *Adv. Sci.*, 2021, **8**, 2004643;
**50** B. Unlu et al., *Addit. Manuf.*, 2024, **94**, 104455;
**51** A. Grabulosa et al., *Nanophotonics*, 2022, **11**, 1591–1601;
**52** D. S. Miner et al., *Microsyst. Nanoeng.*, 2026, **12**, 66;
**53** Z. J. Geffert et al., *ACS Appl. Mater. Interfaces*, 2024, **16**, 69807–69817;
**54** V. Lagerburg et al., *Ann. 3D Print. Med.*, 2025, **100204**;
**55** D. Torres-Alvarez et al., *Prog. Addit. Manuf.*, 2025, **10**, 2847–2859;
**56** W. Drenckhan & A. Saint-Jalmes, *Adv. Colloid Interface Sci.*, 2015, **222**, 228–259;
**57** Robin R. Benedix, Omar A. Abdelaziz, Alexander Southan, Cosima Stubenrauch; Gelatin-Based Materials with Inverse Structures: Porous Hydrogels Compared to Hydrogel Particles. *Int. J. Biol. Macromol.*, revisions in preparation;
**58** D. Doppler, *Lab on a Chip*, 2023, **23(13)**, 3016–3033;
**59** A. Barbetta et al., *Biomacromolecules*, 2009, **10.12,** 3188-3192.
**60** A. D. Aladese *et al.*, *BioChip Journal*, 2021, **15**, 313–333;
**61** R. Su *et al.*, *Lab on a Chip*, 2023, **23**, 1279–1299;
**62** N. Weigel et al., ACS Applied Materials & Interfaces, 2021, **13**, 31086–31101;
**63** H. Shan *et al.*, *Small*, 2023, **19**, 2205498;
**64** H. J. McLennan *et al.*, *Scientific Reports*, 2023, **13**, 562;
**65** D. Gonzalez-Hernandez *et al.*, *Advanced Optical Materials*, 2023, **11**, 2201701;
**66** L. Chen et al., Microsystems & Nanoengineering, 2025, **11**, 10;
**67** F. Cantoni et al., Advanced Materials Technologies, 2024, **9**, 2300718;
**68** J. Schindelin et al., *Nature Methods*, 2012, **9(7)**, 676–682;
**69** C. Claaßen et al., *Biomacromolecules*, 2018, **19**, 42–52;




View Article Online
DOI: 10.1039/D6LC00261G

## Data availability statement

The data supporting this article have been included as part of the supplementary information (SI). Supplementary information is available. See DOI: